Exp Fluids (2013) 54:1419
DOI 10.1007/s00348-012-1419-9

RESEARCH ARTICLE

Phase discrimination and object fitting to measure fibers distribution and orientation in turbulent pipe flows

Stella S. Dearing · Marina Campolo · Alessandro Capone · Alfredo Soldati

Received: 6 February 2012 / Revised: 12 October 2012 / Accepted: 15 October 2012

Abstract In this work, a methodology based on the analysis of single-camera, double-pulse PIV images is described and validated as a tool to characterize fiber-dispersed turbulent flows in large-scale facilities. The methodology consists of image pre-treatment (intensity adjustment, median filtering, threshold binarization and object identification by a recursive connection algorithm) and object-based phase discrimination used to generate two independent snapshots from one single image, one for the dispersed phase and one for the seeding. Snapshots are then processed to calculate the flow field using standard PIV techniques and to calculate fiber concentration and orientation statistics using an object-fitting procedure. The algorithm is tuned and validated by means of artificially generated images and proven to be robust against identified sources of error. The methodology is applied to experimental data collected from a fiber suspension in a turbulent pipe flow. Results show good qualitative agreement with experimental data from the literature and with in-house numerical data.

S. S. Dearing · M. Campolo · A. Capone · A. Soldati (✉)
Centro Interdipartimentale di Fluidodinamica e Idraulica, Università degli Studi di Udine, 33100 Udine, Italy
e-mail: soldati@uniud.it

S. S. Dearing
e-mail: stella.dearing@uniud.it

M. Campolo
e-mail: marina.campolo@uniud.it

A. Capone
e-mail: alessandro.capone@uniud.it

A. Soldati
Department of Fluid Mechanics, International Center for Mechanical Sciences, 33100 Udine, Italy

1 Introduction

Fiber suspensions in turbulent flows are commonly encountered in a wide range of industrial applications. Examples include pulp production, papermaking processes and several other industrial applications in which fibers should be processed (e.g., fiber drying) or used as drag reducing agents (Paschkewitz et al. 2005). Controlling the rheological behavior and the concentration/orientation distribution of fibers is pivotal for process optimization. In papermaking processes (Lundell et al. 2011), mechanical properties of manufactured paper are deeply influenced by anisotropic fiber orientation induced by the carrier flow. In fluid transport systems [see Paschkewitz et al. (2005) and Gillissen (2008) among others], elongated fibers interacting with turbulent structures in the wall layer can be a valuable alternative to flexible polymers for reducing pressure drops.

Due to the practical importance of such suspensions, various experimental (see Carlsson et al. 2007; Holm and Soederberg 2007; Krochak et al. 2008; Parsheh et al. 2005, 2006 among others) and numerical works (see Zhang et al. 2001; Mortensen et al. 2008a, b; Marchioli et al. 2010) have been carried out to study fiber dispersion in internal flows.

Experimental and numerical works have shown that fibers accumulate in the viscous sublayer and preferentially concentrate in regions of low-speed fluid velocity tending to align with the mean flow direction, in particular close to the wall. A step forward was taken by Krochak et al. (2009), who investigated by numerical simulations phase coupling in fiber suspensions flowing in a tapered channel and in Poiseuille flow (Krochak et al. 2010).

Numerical works rely heavily on the broad assumptions required to model fiber motion in a computationally

Published online: 21 December 2012

efficient and physically representative way. Validation of such assumptions demands a thorough characterization of the flow in terms of fiber orientation and distribution. More experimental data on such flows are needed to provide benchmark data for future modeling and approximate simulation methods (Marchioli et al. 2008).

In this work, we describe, validate and finally apply a comprehensive methodology based on simultaneous single-camera two-phase PIV measurements to obtain information about orientation and distribution of fibers together with flow field data in a turbulent pipe flow.

The application of standard laboratory techniques at scales of industrial interest is not straightforward since (1) two-phase PIV parameters need to be tuned to the specific setup used to make measurements and (2) major disturbances may arise from the industrial-type environment.

Optical measurements have been extensively used to characterize fiber suspension flow. Parsheh et al. (2005) used high-speed imaging and Laser Doppler velocimetry to study the orientation of fibers in a planar contraction. Metzger et al. (2007) developed a procedure to perform PIV calculations directly on fiber images for fibers sedimenting in a viscous fluid at low Reynolds number. Moses et al. (2001) used image-processing to investigate fiber motion near solid boundaries in a simple shear flow. When the objective is the simultaneous measurement of the dispersed phase and the carrier fluid in dilute two-phase flow, more elaborated PIV approaches should be used. The simultaneous characterization of the continuous phase and the dispersed phase can be obtained using two synchronized cameras and fluorescent tagging: The light scattered by both phases is recorded by one camera, while the other camera records only fluorescent images [see Cheng et al. (2010) for a detailed review of two-cameras methods]. Alternatively, when only one single camera is used, phase discrimination can be obtained based on image intensity, spot size or shape or even based on the relative difference in motion of the two phases [see Khalitov and Longmire (2002) for a detailed review]. These techniques proved to be successful at the laboratory scale under specific testing conditions (i.e.. when the seeding and the dispersed phase are sufficiently different in size, in inertia or in geometrical properties to be discriminated correctly). In this work, we need to identify and validate a cheap, reliable image-processing technique which is robust enough to discriminate between fibers and seeding in the fully developed turbulent flow inside a pipe in order to characterize the flow field and to calculate fiber concentration and orientation statistics. The methodology consists of image pre-treatment (intensity adjustment, median filtering, threshold binarization and object identification by a recursive connection algorithm) and object-based phase discrimination used to generate two independent snapshots from one single image, one for the dispersed phase and one for the seeding. The performance of each image pre-treatment processing step is controlled by specific parameters, whose value is strongly sensitive to the test experimental setup: The minimum size of the tracer/fiber in the image dictates the maximum size of the median filter which can be used to remove the background noise without removing also tracer/fibers from the image; the relative difference between tracer/fiber dimension determines the level of complexity of the phase discrimination step; the fiber aspect ratio determines the most reliable technique to identify fibers and to calculate their orientation.

Furthermore, phase discrimination requires non-trivial image-processing steps in order to discriminate the dispersed phase from the carrier flow seeded with particle tracers (see Kiger and Pan 1999; Cheng et al. 2010). Different methods for fiber identification and subsequent orientation measurement have been implemented in various works. In Bernstein and Shapiro (1994) fibers detection and fiber orientation assessment were achieved through a visualization technique consisting of a short-duration 3D video-photography system. However, typical bi-dimensional PIV systems feature a single camera and orientations must be calculated directly from a single image. In the work by Parsheh et al. (2005), the authors investigated the fiber orientation distribution function at the centerline of a planar contraction using an object-fitting technique.

In Carlsson et al. (2007), authors investigated fiber orientation in a flow over an inclined plane using a second-order ridge detector with steerable filters [adapted from Jacob and Unser (2007)] for the calculation of fiber position and orientation in both streamwise and crosswise planes. Carlsson et al. (2011) build on these results, comparing the ridge detector to an elliptic filter using data from a fiber suspension in a laminar shear flow, finding that the two methods achieve approximately the same accuracy in spite of a lower computation time demanded by the ridge detector. With the same setup and methodology, Kvick et al. (2010) measured fiber position and orientation in relation to the low-speed streaks present in a turbulent boundary layer.

In this work, we develop and validate a robust fiber identification and orientation calculation algorithm that is suitable for simultaneous PIV applications in our specific test environment in which (1) the (lower) size of the dispersed phase (fiber diameter) is similar to the size of the tracer and (2) the fiber aspect ratio is not very large (order 10). When the fiber aspect ratio is small, edge detection as used by Rose et al. (2007, 2009) becomes quite difficult to apply. The methodologies proposed by Metzger et al. (2007) and by Moses et al. (2001) to calculate fiber orientation become also difficult to apply. In Metzger et al. (2007), the typical fiber length was large (80 pixels); in

Moses et al. (2001), the aspect ratio of fibers was also quite large 40–60. In fact, fiber images size should be as big as possible in order to get good results when fiber orientation is measured based on the orientation of the line connecting the two ends of the fiber.

Since our object is to process a large number of images as required in a PIV-like context to derive joint statistics of flow field and dispersed phase (fiber) distribution and orientation, also the costs associated with image processing may become a major concern. Carlsson et al. (2007, 2011) used convolution of the fiber images with a steerable filter to detect fiber orientation. This algorithm is likely to be computationally more expensive than the algorithm (ellipse fitting-based) we propose in this work.

In Sect. 3, a detailed description of each image-processing step of the algorithm is given, with a focus on phase discrimination and fiber orientation detection. Details about the image pre-filtering processing steps are discussed in the "Appendix". A key aspect of this work is the algorithm validation process, which is fully described in Sect. 4. In Sect. 5, results of the application of this methodology to experimental data gathered on the large-scale facility along with sample PIV velocity fields are shown and compared on a qualitative basis to the literature data.

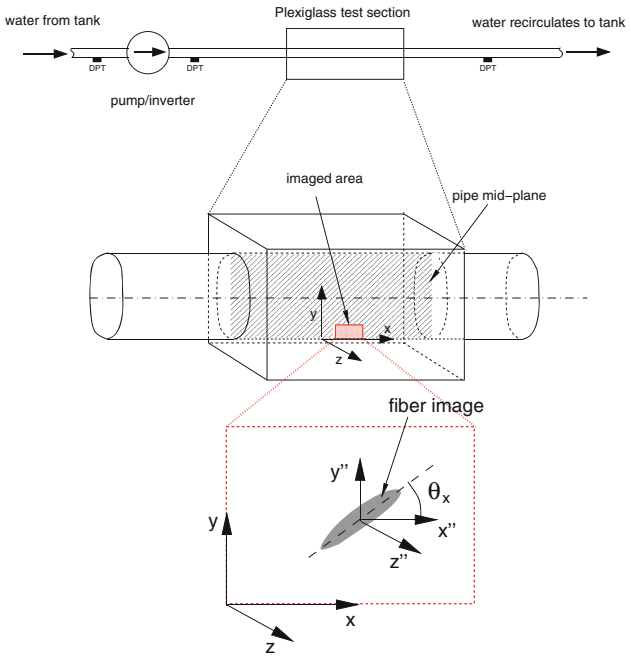

Fig. 1 Schematic of the experimental facility. DPT is differential pressure transducer. Imaged region is shown in *red*. Angle θ_x is used to determine fiber orientation with respect to a comoving frame (x'' , y'' , z'') with origin in the fiber's center of mass and parallel to the inertial frame of reference

2 Experimental facility

The experimental facility consists of a closed loop pipe with circular section of $D = 0.10$-m internal diameter and a total working length of $\simeq 30$ m. The working fluid (water) is supplied by a centrifugal pump connected to a frequency inverter, which allows flow rate control. A schematic of the setup is shown in Fig. 1. The test section is made of Plexiglass in order to allow visual access and consists of a 2-mm-thick pipe surrounded by a box filled with water. The pipe wall thickness inside the test section is thinner than in the rest of the pipe loop. This feature reduces image distortion due to refraction resulting from the curved geometry of pipe which acts like a lens, whereas the water-filled box helps minimize image distortion due to refraction resulting from change in material (plexiglass/water) occurring at the pipe interface.

Pressure drop data are collected by a pair of differential pressure transducers (DPT). Flow and fibers visualization was achieved by means of an imaging system comprising a pulsed Nd: Yag laser ($\lambda = 524$ nm), optics for the light sheet shaping whose thickness was set to 1 mm, a 1,280 × 1,024 PCO Sensicam camera with a Nikon F 50 mm ($f = 1.4$), a frame grabber and PC for image acquisition and analysis. Experiments were carried out at Reynolds number ($Re = UD/\nu$ where ν is the kinematic viscosity of the fluid, U is the fluid bulk velocity, and D is the pipe diameter) equal to $Re = 8{,}043$. Flow seeding was attained with 20-μm diameter hollow glass spheres, whereas nylon fibers (Polyamide 6.6, density 1.13–1.15 g/cm^3 produced by Swissflock AG) with a mean length of approximately 320 μm and mean diameter 24 μm were employed as dispersed phase (see Fig. 2).

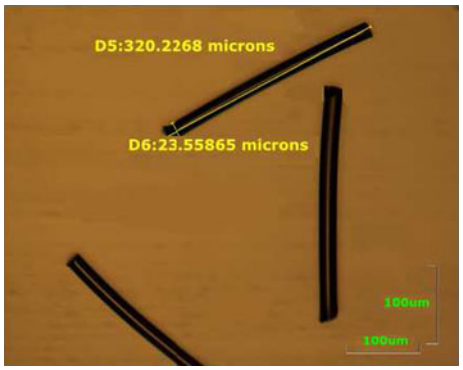

Fig. 2 Fibers microscopic image. Diameter and length of a sample fiber are given

Fiber concentration expressed as mass fraction was $C = 0.01$ %. Non-interacting suspensions are characterized by $nL_f^3 \ll 1$, where n is the number density of fibers, and L_f is the fiber half-length. The fiber suspension

presented in this work is characterized by $nL_f^3 = 0.02 \ll 1$ indicating dilute flow conditions.

The imaged area (shown in red in Fig. 1) was a 17 mm × 21 mm region lying on the vertical plane through the pipe axis and covering the near-wall region of the flow. A series of 800 images was collected with an acquisition rate of 15 Hz.

PIV calculations were performed using a commercial software (DaVis by LaVision Gmbh). The image-processing algorithm was implemented using Matlab routines.

3 Description of image-processing algorithm

Figure 3 shows a sample snapshot of fiber and seeding particles taken from our pipe testing section. A close-up of the picture is shown on the right. The close-up covers a 5.6 mm × 6 mm area (about 1/9 of the full image) and yet shows many of the features affecting image quality in the system under investigation. The simultaneous presence of seeding particles (appearing as white dots and indicated by the green arrows) and fibers (elongated white regions) is clearly noticeable. Sources of noise and image quality decay are introduced by the optical interactions between fibers and particles. Fiber diameters have dimensions of the order of the seeding particles, hence fibers which are perpendicular to the laser sheet (as those indicated by yellow arrows) will not be distinguishable from seeding particles.

Another issue is the presence of out of focus fibers and fibers lying in front of laser sheet which cause shadows to appear (indicated by blue arrows). These regions are characterized by little or no seeding particles. The last issue is that of partially overlapping fibers, as those indicated by red arrows. Image quality is undermined by all these different concurring effects and image processing is required to minimize these disturbances.

The whole image-processing algorithm is composed of four main steps, that is, image pre-processing, phase discrimination, fiber analysis by object fitting and PIV analysis. A detailed description of the algorithm is described in the following sections.

3.1 Pre-processing

Raw images of laser-illuminated fibers must be pre-processed to remove the background noise. In this work, this is made in three steps: First, the image intensity is adjusted such that 1 % of the pixels is saturated at lowest and highest intensities of the original image. This increases the contrast of the output image and makes the fibers appear brighter. Second, high-frequency noise is eliminated using a 3 × 3 pixels median filter. Larger values of filter size prove to introduce a filtering effect on tracer images [as described in Kiger and Pan (2000)] without significant advantages in noise removal. Third, images are binarized: Every pixel value above a prescribed intensity level (230) is set to a maximum (255), and every pixel below this value is set to zero. Once the image is binarized, phase discrimination can be carried out. Details on the implementation of each image pre-treatment step and criteria for the tuning of the parameters involved by the processing algorithm are briefly discussed in "Appendix".

3.2 Phase discrimination

The features of connected bright regions showing in each binarized image are evaluated using a recursive connectivity algorithm. Information about the size and the aspect ratio of each identified region, or object, is stored and can be employed to assess whether the object represents a tracer particle or a fiber. In this work, in order to identify

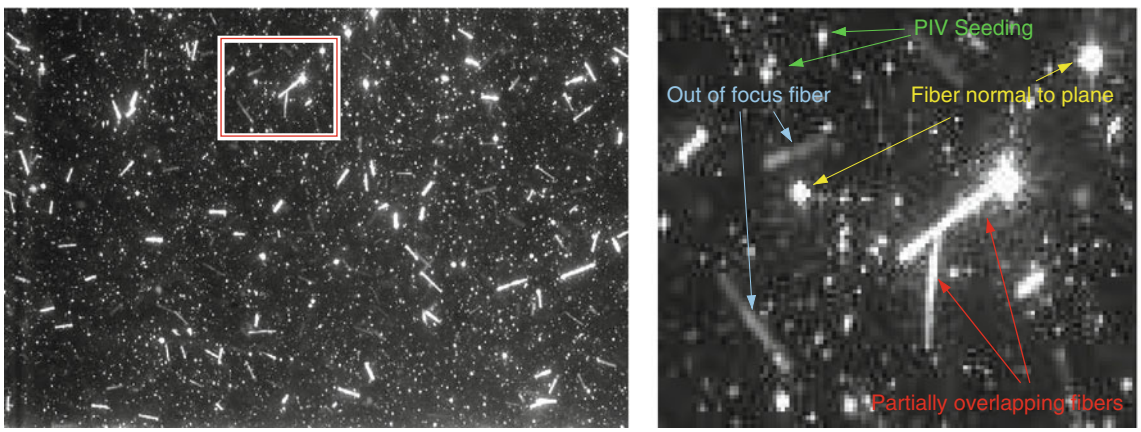

Fig. 3 Sample raw image with tracer particles and fibers (*left*) and selected area (*red square*); close-up of selected area (*right*) with shadows of out of focus fibers (indicated by *blue arrows*), partially overlapping fibers (indicated by *red arrows*), PIV seeding particles (indicated by *green arrows*) and fiber normal to image plane (indicated by *yellow arrows*)

image objects representing fibers, we applied first an aspect ratio threshold discarding all the image objects featuring an aspect ratio lower than 1.5. Also, setting an aspect ratio threshold may be useful to eliminate both deformed, highly curved fibers and intersecting fibers from the identification process when this becomes a critical issue in the experiment. Secondly, objects with a length exceeding a threshold value $l^* > 1/7\ l$ where l is the fiber length (see Table 1 for details) were considered as fibers. The criteria underlying the choice of the threshold value are discussed in detail in Sect. 4.3

A set of pictures describing the pre-processing and phase discrimination steps is shown in Fig. 4. Figure 4a depicts a close-up of a raw image of 140 × 200 pixels (approximately 2 mm × 3 mm actual size) where seeding particles and fibers are clearly visible. Figure 4b is the output of the filtering and binarization step carried out on the raw image. As described, image is then fed to the recursive connectivity algorithm to identify the features of the image objects. Finally, Fig. 4c shows image objects which have been identified as fibers according to the mentioned criteria on aspect ratio and size.

Table 1 Effect of threshold length, l^*, on mean direction cosine relative error

Threshold length	$\lvert\cos(\theta_x)\rvert$	Relative error on $\lvert\cos(\theta_x)\rvert$ (%)
$l^* > 1/9\ l_f$	0.61	4.4
$l^* > 1/7\ l_f$	0.64	0.5
$l^* > 1/3\ l_f$	0.66	3.5
$l^* > 2/3\ l_f$	0.677	5.96
$l^* \approx l_f$	0.698	8.8

l_f represents fibers actual length. Test case 2, error calculated over 45,000 fibers

3.3 Fiber analysis by object fitting

Images in which fibers have been identified may then be further processed to obtain information about fiber orientation. To this end, image regions sorted as fibers are fitted to geometric ellipses following a non-linear least square approach as described in Fitzgibbon et al. (1999). Ellipses were chosen because they reproduce quite reasonably the behavior of rigid elongated fibers in a number of applications of both scientific and engineering interest (Marchioli et al. 2010).

Given a set of N points (x_i, y_i), $i = 1, 2, \ldots, N$, with (x_i, y_i) representing the coordinates of the center of each pixel associated with the image object identified as a fiber, a fitting conic is described by a second-order polynomial:

$$F(x,y) = a_{11}x^2 + a_{12}xy + a_{22}y^2 + 2a_{13}x + 2a_{23}y + a_{33} = 0 \quad (1)$$

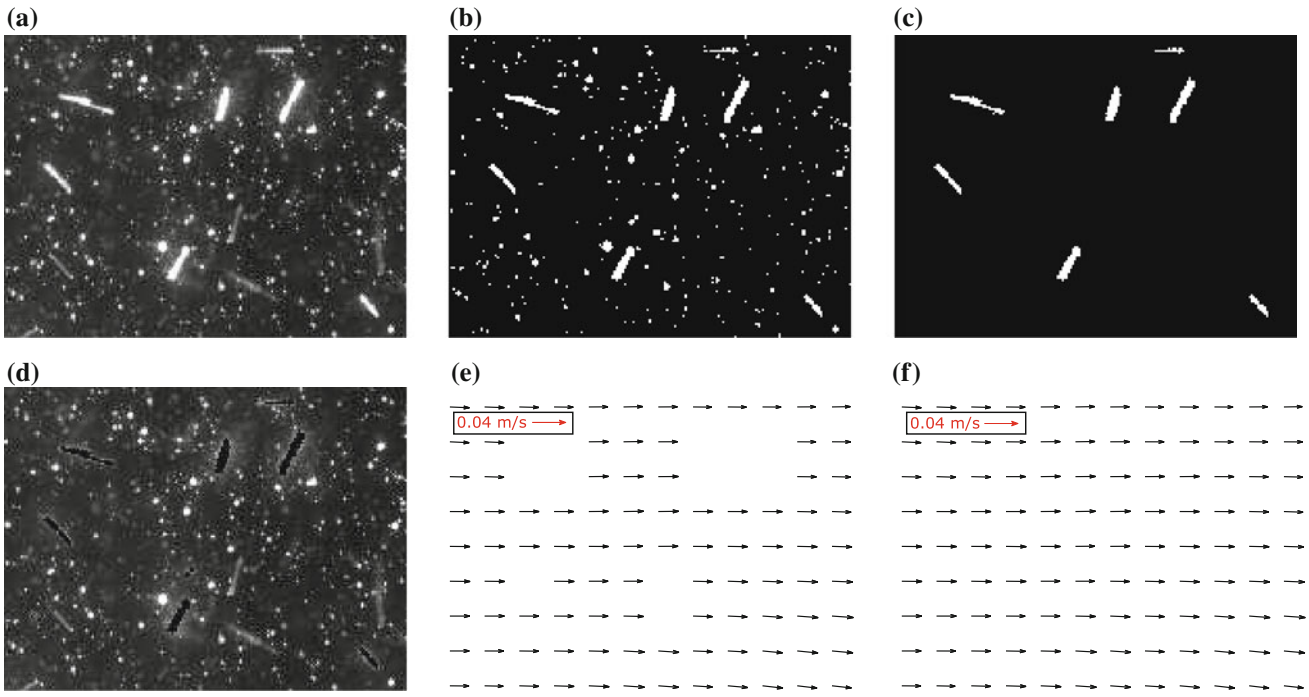

Fig. 4 Steps of image-processing algorithm: raw image, pre-processing and phase discriminated fibers (*top*); seeding only image and PIV analysis

The fitting conic is an ellipse if coefficients a_{ij} satisfy the specific constraint:

$$a_{12}^2 - a_{11}a_{22} < 0. \quad (2)$$

Values of a_{ij}, $i = 1, 3; j = 1, 3$ can be estimated using a general least-squares fitting approach which minimizes the sum of the squared algebraic distances of the N points to the generic conic [see Fitzgibbon et al. (1999) for details].

Once the best fitting ellipse in terms of coefficients a_{ij} is computed, the orientation and all other relevant fiber statistics are calculated from the values of a_{ij}. For instance, rotation is calculated from coefficient a_{12}, which represents the tilt of an ellipse in the x–y plane. Fiber orientation, θ_x, is defined as the angle formed by the best fitting ellipse major axis and the streamwise axis x, as depicted in Fig. 1. Using simple algebra, the coefficients a_{ij} can also be used to code the information about the fiber center of mass, aspect ratio and length as derived from the 2D image.

3.4 PIV analysis

For a simultaneous PIV system to be implemented though, also images of particle-seeded flow are necessary. To obtain such pictures, a straightforward method was employed that is, fibers-only images were subtracted from the intensity-adjusted/median-filtered images, thus leading to images displaying only particle tracers (see Fig. 4d). The resulting images are thus suitable for PIV processing.

The reason why this procedure was preferred to object detection to identify seeding particles is twofold. First, fibers are considerably brighter than seeding particles and the region surrounding fibers is immersed with residual gray pixels which blur particles lying within this region. This is known as the corona effect and has been reported for spherical particles in Sakakibara et al. (1996) and is one of the main causes of spurious velocity measurements. Second, since fibers which are not perfectly in focus do not have an uniform gray level nor are bright, they may result broken after binarization and appear like seeding particles, producing spurious vectors in the PIV processing phase.

PIV processing was performed using a commercial software. The advanced image deformation multipass PIV cross-correlation algorithm with window offset, adaptive window deformation and Gaussian subpixel approximation was used (see Stanislas et al. 2008). Minimum window size was set to 32 × 32 pixels with an overlap of 50 % leading to a distance between vectors of 16 pixels corresponding to 0.3 mm. Figure 4e, f show the typical output of PIV processing. In Fig. 4e, the effect of fiber removal on PIV results has been highlighted discarding the velocity vectors when the correlation peak ratio was below 4, leading to no data areas in the regions where fibers were removed. Figure 4f shows the vector field obtained when the mentioned threshold on correlation peak ratio was set to 3.

4 Validation of image-processing algorithm on synthetic experiments

Experimental two-phase simultaneous PIV investigations of fiber-laden turbulent flows are prone to various sources of error which should be adequately assessed and estimated. In particular, the fiber identification and orientation calculation process described in the previous section are subject to several limitations. First of all, distribution and orientation statistics are calculated only considering detected fibers. This means that fibers which are aligned or nearly aligned to the z axis and feature small orientation angles with respect to streamwise direction will be most likely not identified in the phase discrimination step and, therefore, will not be included in the calculations. In the limiting case, fibers perpendicular to the x–y plane will look like a dot and thus invisible to the detection algorithm. Second, fibers that are only partially illuminated by the laser sheet could be misinterpreted as seeding or impurities. Finally, special attention should be paid to the intrinsic approximation of using two-dimensional image information which are indeed the projection of three-dimensional orientation data. In this and similar works where images are collected with a single camera, fiber orientation data are in fact worked out from projections of three-dimensional fibers onto the bi-dimensional image plane, and the effect of such process should be carefully accounted for.

When fiber length distribution is narrow enough (i.e., all fibers have the same length, l_f) and the laser sheet thickness, Δz, is known, 2D orientation data can be used to evaluate the 3D orientation using simple algebra. Indicated with $\theta_{x,2D}$ the fiber orientation in the laser image plane calculated as $|\cos(\theta_{x,2D})| = l_x/(l_x^2 + l_y^2)^{0.5}$ where l_x and l_y are the projected length of the fiber image along x and y directions, the 3D orientation can be calculated as:

$$|\cos(\theta_{x,3D})| = |\cos(\theta_{x,2D})| \frac{(l_x^2 + l_y^2)^{0.5}}{(l_x^2 + l_y^2 + \delta^2)^{0.5}} \quad (3)$$

where $\delta = \Delta z$ if $l_x^2 + l_y^2 < l_f^2 - \Delta z^2$ or $\delta = l_f^2 - (l_x^2 + l_y^2)$ if $l_x^2 + l_y^2 > l_f^2 - \Delta z^2$.

With reference to PIV velocity fields calculation, it is necessary to assess the error introduced by the "holes" left by fibers' image removal.

Monte Carlo simulations were adopted in this work to quantify the error magnitude affecting fibers number density and orientation distribution results. These simulations provide pseudo-experiment information on fiber distribution and orientation within the laser sheet. Artificial images

which contain a certain number of seeding particles and randomly oriented fibers are generated automatically and subsequently fed to the phase detection and fiber orientation modules. Statistical reliability is ensured by the large amount of data employed over the process, whereas the way artificial images are generated is aimed at simulating the sources of uncertainty previously detailed. Two main test cases have been setup to validate the algorithm, each one characterized by specific image features as described below:

1. Artificial images displaying 50 or 150 fibers featuring no spanwise orientation (all fibers lying entirely within planes parallel to x–y plane)
2. Artificial images displaying 150 fibers featuring spanwise orientation

In all test cases, fiber aspect ratio in the artificial images has been set to 20. Each test case has been run several times by gradually increasing the number of images and consequently the number of fibers, to assess the effect of fiber sample size on the accuracy of the calculated statistics. Finally, the effect of the length threshold on the accuracy of the fiber identification step has been quantified.

4.1 Artificial images generation

Artificial images have been generated to account for the several sources of uncertainty which exist in actual experimental conditions. First of all, the light source is provided by a laser sheet having a finite thickness which implies that fibers could possibly be only partially lit thus leading to inaccuracy in the detection phase. The light intensity is also not uniform along the laser sheet thickness, resulting in non-homogeneously illuminated fibers. Images have been thus obtained generating first an artificial volume in which fully three-dimensional fibers and seeding particles have been randomly generated and subsequently taking into account just a thin slice of the volume. The objects, that is, fibers and seeding particles, contained within the obtained sub-volume are then projected onto a plane. This method makes it possible to mimic the laser sheet thickness effect on algorithm accuracy along with the effect of estimating object orientation in a three-dimensional space from the two-dimensional data. Fiber objects have been simulated by ellipsoids with same fixed dimensions and have been placed randomly in the artificial volume applying to them a random three-dimensional rotation matrix; seeding particles were considered as spherical objects distributed randomly inside the artificial volume. Light intensity distribution of tracer particles is calculated based on the relation described in Raffel et al. (2002) which has been extended to ellipsoid-like objects. For the generic fiber depicted in Fig. 5, light intensity along fiber minor axis in the region included between the two focal points of coordinates (x_{f1}, y_{f1}) and (x_{f2}, y_{f2}) is assumed to be constant. In the same region, the intensity along fiber major axis is instead assumed to follow a Gaussian profile, described as

$$I(x') = I_0 \exp\left[\frac{-(x' - x_0)^2}{\frac{1}{8}d_\tau^2}\right] \tag{4}$$

where (x_0, y_0), d_τ and I_0 represent, respectively, the coordinates of ellipsoid center, the ellipsoid image length and laser sheet peak intensity. At the ellipsoid's ends, in the region where $x_{f1} \geq x \geq x_{f2}$ holds, light intensity is considered to be dependent on both coordinates leading to the following relation

$$I(x', y') = I_0 \exp\left[\frac{-(x' - x_{fi})^2 - (y' - y_{fi})^2}{\frac{1}{8}d_\tau^2}\right] \tag{5}$$

where (x_{fi}, y_{fi}) is the generic focal point coordinate. The value d_τ represents the particle image diameter which accounts for diffraction limited and geometric spot size (Raffel et al. 2002) and is determined considering the following relations

$$d_\tau = \sqrt{M^2 d_p^2 + d_s^2} \tag{6}$$

$$d_s = 2.44(1 + M)f\lambda \tag{7}$$

where d_p represents the physical particle size, M the lens magnification, approximately 0.4 in this work (Raffel et al. 2002), d_s is the diffraction limited spot size and $f = 1.4$ and $\lambda = 524$ nm are optical system parameters. Peak intensity of the laser sheet I_0 is non-constant within the laser sheet, resulting in inhomogeneous lighting of fibers lying within the sheet. The peak intensity depends on the actual position of fiber within the sheet, leading to the following expression for I_0

$$I_0(z) = q \exp\left[\frac{z^2}{\frac{1}{8}\Delta z_0^2}\right] \tag{8}$$

where z-axis origin is considered to be at the center of the laser sheet where light intensity is maximum, Δz_0 is the

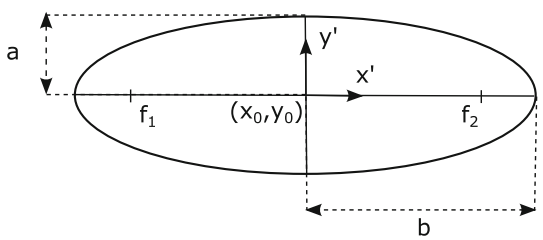

Fig. 5 Single fiber model for light intensity calculation. Focal points are labeled f_1 and f_2

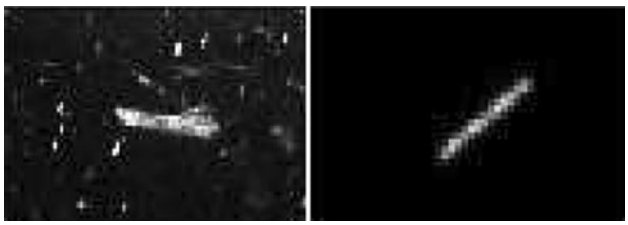

Fig. 6 Sample actual (*left*) and artificial (*right*) fiber images

laser sheet thickness, and q is the efficiency with which the particle scatters light. In Fig. 6 a sample artificial fiber image (right) is compared to an actual one (left).

4.2 Accuracy of ellipse fitting statistics

4.2.1 Test case 1

This case represents the baseline test with fibers orientations defined in x–y plane only. Fibers are located randomly inside the three-dimensional volume and oriented randomly in the x–y plane. Two runs of this test case have been performed: the first is characterized by each artificial image displaying 50 fibers; in the second run, fiber number per image has been increased to 150. In the first case, a very dilute suspension could be simulated, in which no fiber image intersection would occur. By increasing the concentration to 150 fibers a dilute suspension could still be simulated where fiber images intersection would occur, then resembling actual experimental conditions for fiber suspensions in turbulent flow.

Figure 7 shows a close-up of a sample image from the 50 fibers per image case, in which fibers detected with the presented methodology are depicted along with their center of mass. To validate extensively the proposed algorithm, statistics of fiber number density and fiber direction cosine have been computed and compared to expected values. The normalized number density is defined binning (i.e., counting) identified fibers inside regions of constant volume. When a dependence from one spatial coordinate is expected (e.g., the wall-normal direction y in a boundary layer flow), volumes are arranged to span different value of the y coordinate. Dividing the number of fibers in each bin by the overall number of fibers in the image (about 60 fibers per square centimeter), the normalized number density obtained represents a probability density function and its integral equals to 1. Values of fiber number density calculated for artificial images were quite good, with approximately 99.9 % of generated fibers correctly identified and located. The normalized average fiber number density, calculated binning the fibers into 17 discrete slabs arranged in the y direction, was 0.0588 ± 0.0005.

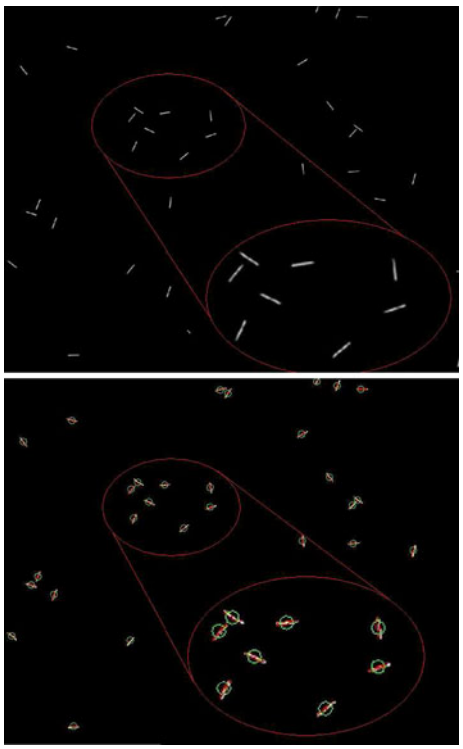

Fig. 7 Close-up of artificial image with 50 fibers (*top*) and detected fibers (*bottom*). *Red contours* and *green circles* show, respectively, the best fitting ellipse and center of mass

Statistics on fiber orientation are obtained in terms of average value of direction cosine, $|\cos(\theta_x)|$. The average value can be calculated considering the whole volume. Nevertheless, when the objective is to define a spatial profile for fiber orientation, the average value can be calculated considering sub regions specifically defined to span different values of the relevant coordinate (e.g., y). Dividing the region of interest in I identical bands along the y direction, the orientation cosines of all the fibers whose centroid lies within the ith band are summed over and then divided by the overall number of fibers. The mean direction cosine at every ith band expressed in y position is thus calculated as

$$\langle |\cos(\theta_x)| \rangle_i = \frac{1}{N_{p,i}} \sum_{k=1}^{N_{p,i}} |\cos(\theta_x)|_k \tag{9}$$

where $N_{p,i}$ represents the number of fibers identified within the ith band. Values of $|\cos(\theta_x)| \simeq 1$ denote a strong mean alignment of fibers to the streamwise direction.

The expected mean direction cosine calculated from artificial images was $2/\pi \approx 0.64$, which is the mean orientation angle projected on a unit sphere for randomly rotated fibers. The mean direction cosine calculated from ellipse fitting of 250 artificial images containing 50 fibers each was 0.64 ± 0.02 (mean $\pm$ standard deviation).

For the test case 1, in which 50 fibers per image were generated, the relative error in $|\cos(\theta_x)|$ is less than 1 % if the number of processed fibers is $O(10^4)$, that is, the number of processed images is large enough to be statistically representative of average fiber orientation.

The second run of the test case, in which 150 fibers were generated per image, made it possible to simulate a more practical flow condition, in which fiber intersection occurs within images, adding a further source of uncertainty in fiber discrimination and orientation calculation due to overlapping fibers. The relative error of calculated mean direction cosine with respect to expected value $2/\pi$ is reported in Fig. 8 versus the number of fibers over which statistics are calculated (i.e., fiber sample size). Validation results confirmed the algorithm accuracy and robustness: A mean direction cosine relative error of 1 % was achieved already after processing 12,500 fibers, corresponding to nearly 85 images.

4.2.2 Test case 2

In this test case, fibers were generated with a random orientation in the three-dimensional volume, that is, without forcing them to lie parallel to the x–y plane. This test case gives information on algorithm robustness toward orientation estimate errors due to fibers featuring weak orientation in the x–y plane as opposed to strong orientation in x–z plane. Artificial images were generated containing 150 fibers each; different runs with increasing number of images were tested to assess the dependency of algorithm accuracy on overall number of fibers sampled. Validation gave satisfactory results, with number density data in good agreement with the expected uniform value. For fibers randomly oriented in the three-dimensional space, expected mean direction cosine should be equal to 0.5. Nevertheless, since statistics are calculated for (the portion of) fibers which are partially illuminated by the laser sheet, calculated mean direction cosine is typically larger than 0.5 because fibers which are strongly orientated out of the image x–y plane are difficult to detect and, in the limiting case, appear as dots and are not even discriminated as fiber. Even in this case, convergence in accuracy is achieved quite fast: $|\cos(\theta_x)|$ relative error calculated for a fiber sample size equal to 1,500 is as much as 5 %; it drops to below 1 % as the total number of fibers reaches 45,000. Figure 8 shows results of test case 2 in comparison with test case 1.

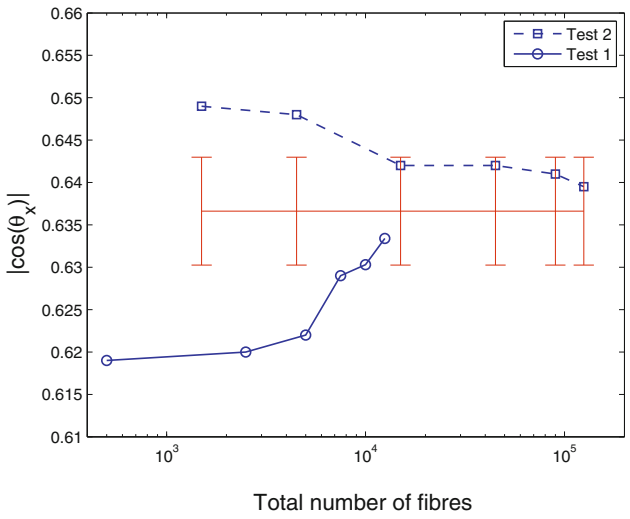

Fig. 8 Mean direction cosine versus number of fibers sampled. Test case 1 and test case 2 compared to expected $2/\pi$ value, *red line* with 1 % *error bar*

4.3 Effect of threshold setting

Two parameters are used to identify fibers within the phase discrimination step, that is, image object's aspect ratio and length. Accurately setting the threshold for the latter can result in significant improvement in algorithm accuracy in terms of $|\cos(\theta_x)|$ relative error. Proper threshold setting involves a certain degree of compromise. More conservative choices, such as deeming as fibers-only image objects having a length equal to actual fiber length l_f, could lead to too many overseen fibers; on the other hand, too loose a threshold would eventually lead to many false positives.

In Table 1, the comparison of results obtained by considering four different length thresholds, l^*, is given. Artificial images used for validation purpose were those from test case 2 (300 images with 150 fibers each). As may be noticed, a strict constraint on image object length compared to actual fiber length, l_f, ($l^* \simeq l_f$) leads to almost 10 % error in $|\cos(\theta_x)|$ calculation. Error decreases steadily when threshold length is set to $l^* = 1/3\ l_f$ of actual fiber length as reported in Parsa et al. (2011) and reaches an optimum with $l^* = 1/7\ l_f$. Lowering the threshold below $l^* = 1/7\ l_f$ leads to an increment in error and an overall decay of algorithm accuracy.

4.4 Effect of phase discrimination on PIV results

Experimental data collected with the facility described in Sect. 2 were used to assess the accuracy of PIV velocity field calculated from tracer images obtained from the processing of pipe images.

Figure 9 shows an instantaneous PIV velocity field. The vector field was resampled, showing only one vector for every two vectors in both directions in order to have a clear image. The removal of fibers images leads to holes in tracer only pictures and consequently, as expected, to regions where no velocity vectors are present.

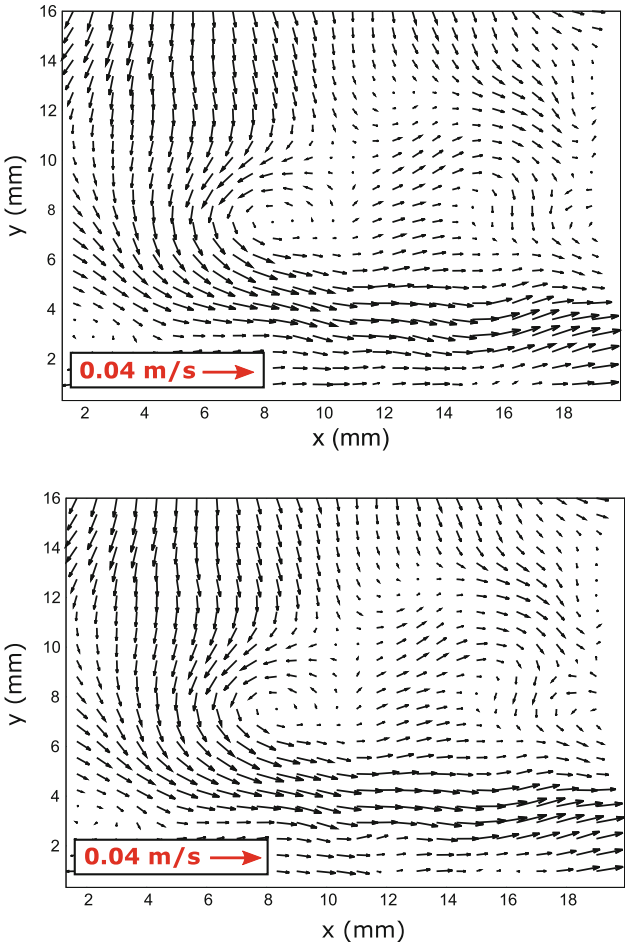

Fig. 9 Phase discrimination validation with respect to PIV calculations: sample field of velocity fluctuations calculated from seeding only image (*top*) and from the same image containing seeding and artificially added fibers after discrimination phase (*bottom*)

A validation of the phase discrimination algorithm was, therefore, performed to assess the error introduced in the PIV calculations by the phase discrimination step. Validation was performed as described in Kiger and Pan (2000) comparing the PIV results from tracer only images to those stemming from the same images to which fibers were artificially added. PIV velocity fields were first calculated from 70 pairs of tracer only images. Composite images displaying seeding and fibers were then generated by combining seeding only images to fibers-only images. The discrimination algorithm was applied to the latter images obtaining seeding only images. PIV calculations were performed on such images and results statistically compared to those collected in the first step.

In Fig. 9, a sample instantaneous field of original seeding only image and a discriminated one are compared. The velocity fields have been obtained subtracting the dominant mean velocity field and show good overall performance. This was confirmed by the computed average error on x, y components, respectively, equal to 0.0042 and 0.0036 pixels. The total error of 0.98 % of the average displacement over the whole field of observation was of the same order of magnitude of that reported in Kiger and Pan (2000).

5 Experimental evaluation of fiber concentration/orientation in turbulent pipe flow

Images of fiber-laden flow recorded from the turbulent pipe were finally examined to calculate concentration/orientation statistics.

Figure 10 shows one sample image and the results of the ellipse fitting phase: red contours represent the ellipses fitting to the fibers, with green circles being the calculated centroids.

Fibers distribution and orientation data obtained from images similar to Fig. 10 have been compared to data from Marchioli et al. (2010).

In the current experimental work, $Re = 8{,}043$ and $Re_\tau = 250$. Re_τ, defined as $u_\tau D/\nu$, is the Reynolds number based on friction velocity, u_τ, and on a relevant dimension (pipe diameter D for experimental data, half-channel width for numerical data). Friction velocity is defined as $u_\tau = \sqrt{\tau_w/\rho}$ where τ_w is the mean shear stress at the wall, and ρ is fluid density. Simulation results from Marchioli et al. (2010) correspond to $Re = 9{,}000$ and $Re_\tau = 150$. Our object in this comparison is to verify a qualitative agreement between current results and previous simulations. Considering (1) the assumptions in the simulations, (2) the difference of the operative parameters and (3) the objective difficulties in examining fibers in wall proximity of a curved pipe, a good qualitative agreement will make us confident that the assumptions of the simulations can be considered a realistic physical model of the reality.

In the simulation of Marchioli et al. (2010), fibers were assumed rigid, with aspect ratios ranging from 1 to 50; the fiber was one way coupled with the fluid and the action of

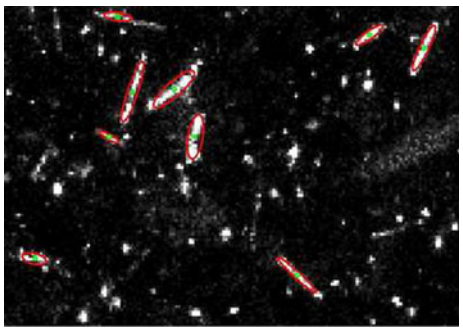

Fig. 10 Fiber fitting ellipses (*red lines*) and centroids (*green dots*) obtained from sample image. $Re = 8{,}043$

the fluid was simulated with a force acting in the fiber's center of mass. In addition, fibers could not interact, and there was no torque exerted by the fluid acting.

To have the closest experimental representation of this idealized simulation, we chose rigid plastic fibers with a similar aspect ratio. Fibers are shown in Fig. 2. We characterized the dimensions of the fibers with a particle size distribution analyzer based on laser diffraction (Horiba Partica LA-950), and we obtained their characteristic sizes. They are all equal, with a very narrow range distribution; they are cylindrical in shape, with a diameter of 24 μm and a length of 320 μm, corresponding to an aspect ratio of 13.6.

Pressure drop readings and velocity data confirm that the flow is fully developed and turbulent and the pipe is smooth. Figure 11 shows the calculated mean wall-normal fiber concentration obtained from the entire 800 images set. Normalized number density is plotted against the distance from the wall expressed in wall units $y^+ = u_\tau\, y/\nu$, where ν is the kinematic viscosity of the fluid.

Fiber number density profile is calculated binning the distance from the wall into 17 slabs. With this choice, an overall number of at least 3,000 fibers could be located in each slab, obtaining smooth number concentration profiles and yet achieving a good resolution. Fiber number density reaches a peak relatively close to the wall, whereas the concentration profile approaches a value of 0.059 (i.e., the uniform value) further away from the wall.

Experimental results confirm on a qualitative basis the profile of normalized number density shown in Marchioli et al. (2010). In the simulations, the concentration profiles flatten in the center of the channel rising in proximity to the wall. Such a peak was explained for spherical particles in connection with the structure of turbulence in the near-wall region (see Marchioli and Soldati 2002). In Marchioli et al. (2010), the peak of fibers' distribution in wall proximity was explained by similar arguments. In current experiments, the concentration profile develops a peak between $y^+ \approx 13.5$ and $y^+ \approx 27$ as noticeable from Fig. 11.

In the simulations, the peak occurs at y^+ between 1 and 2. We should remark here that specific assumptions of non-interacting fibers and the representation of fibers as point-wise are crucial for this result and are known as weak points of such Lagrangian simulations which, ultimately, overpredict the concentration peak and predict its occurrence too close to the wall (Picciotto et al. 2005). It is of some significance to compare present results on orientation against those obtained by the simulations. In Fig. 12, we show the absolute value of 2D mean direction cosine against DNS data discussed in Marchioli et al. (2010). We also plot in the Figure the line corresponding to the mean value of the absolute direction cosine expected for fibers oriented randomly in a two-dimensional space ($2/\pi \simeq 0.64$) and in a three-dimensional space (0.5). Observing the experimental data, we notice that close to the wall, the mean direction cosine values reach almost 0.8. This indicates that, in the wall region, fibers tend to move with a strong alignment with the flowing fluid: This alignment is determined by the action of shear. The direction cosine decreases gradually from the wall region to the outer region until reaching a value in the central region of the channel which is slightly lower than 0.64.

DNS data match with experimental data only in the region between $y^+ = 10$ and $y^+ = 30$. In the region closer to the wall, DNS data predict fiber orientation less aligned with the flow. This datum may be questionable because of

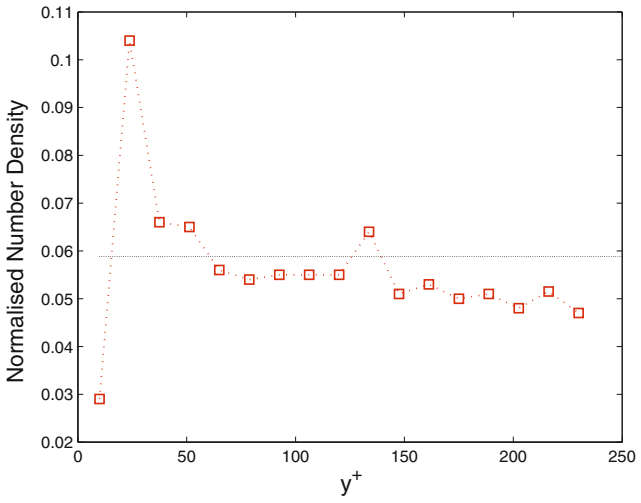

Fig. 11 Fibers number density: experimental data at $Re = 8{,}043$. *Red squares* represent experimental results; *dotted line* means expected normalized number density

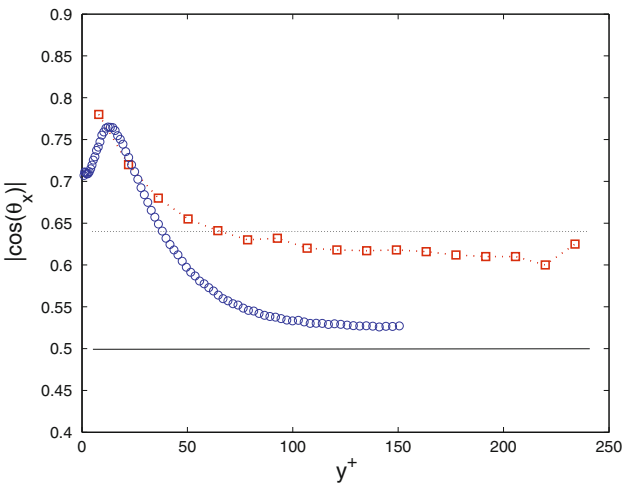

Fig. 12 Fibers mean orientation results: experimental data at $Re = 8{,}043$. *Red squares* represent experimental results, *blue circles* DNS data from Marchioli et al (2010), *dotted* and *solid line*, respectively, expected mean orientation in 2D and 3D

the rather crude assumptions of fiber motion in wall proximity. We remark here also that in the simulations (Marchioli et al. 2010) fibers touch the wall only when their center of mass touches the wall. In reality, fibers which approach the wall in a streamwise-oriented position are likely to coast the wall in the same position, also due to the hydrodynamic interactions with the wall. Beyond $y^+ = 30$, DNS data also tend to underpredict experimental data. They eventually approach a value $\simeq 0.5$ for the streamwise direction cosine: This is exactly the average orientation expected for fibers oriented randomly in the three-dimensional space.

6 Conclusions

A methodology based on the analysis of single-camera, double-pulse PIV images is described and validated as a tool to characterize fiber-dispersed turbulent flow in large-scale facilities.

The methodology includes image pre-processing, object identification, phase discrimination and object fitting for the calculation of fiber distribution and orientation statistics. In the phase discrimination step, objects are sorted according to parametric combinations of length and aspect ratio. The outcome of this process is fiber-only images which can be subtracted to the raw image to obtain seeding particles only image to be processed in a PIV step. The impact on PIV calculations resulting from the presence of fibers has been assessed statistically. Fiber-only images can be further processed using an ellipse fitting algorithm to calculate fibers statistics (number density concentration and orientation). The intrinsic limitations of the image-processing technique have been pointed out, and a validation process has been designed to take into account sources of uncertainties arising in experimental conditions.

The algorithm proved to be robust toward typical sources of error, featuring good convergence behavior and accuracy. Based on these results, the methodology has been successfully employed to obtain fiber concentration and orientation data from a fiber-laden turbulent flow. Simultaneous PIV calculations of the fluid phase have been proven possible. Preliminary experimental results of fiber concentration and orientation obtained for a moderate Reynolds turbulent pipe flow were shown and qualitatively compared to DNS results showing a good match.

Acknowledgments We thank Professor Pietro Poesio for useful discussion and the kind collaboration in making available a small-scale experimental setup. S.S.D. would like to acknowledge Dr. C. Marchioli for the helpful technical discussions in the early stages of the study. Financial support from CIPE Comitato Interministeriale per la Programmazione Economica under Grant "Caratterizzazione ed abbattimento di inquinanti e analisi del rischio nei processi di lavorazione del legno", and from the Regional Authority of Friuli Venezia Giulia under Grant "Nuove metodologie per la riduzione e la gestione di emissioni di COV e particolato per l'industria di pannelli di particelle e fibra di legno" are gratefully acknowledged.

Appendix: Image pre-treatment processing algorithms

Intensity adjustment and contrast enhancement

Images of fiber/particle laden flows acquired by a camera when a laser sheet illuminates the flow can be very different in pixel intensity distribution depending on the specific setup used (laser power, camera) and test conditions (distance of camera). In spite of this, image-processing algorithm must be designed to be robust to changes in light conditions. Therefore, it is common practice to adjust the pixel intensity of the original image, $I(x, y)$, where (x, y) is pixel position in the bi-dimensional image, to span the reference intensity interval 0–255. Some loss of information can be tolerated in this step since the final result should be a set of images characterized by normalized pixel intensity and increased contrast between objects and background.

In this work, we use the probability density function (PDF) of pixel intensity to (1) obtain a compact representation of the image intensity level and to (2) fix intensity thresholds to correct the image to account for variability in light conditions. Irreversible corrections of pixel intensity (such as trimming of image intensities which are above/below some threshold value) should be contained as much as possible to reduce the loss of information during image processing. Intensity thresholds can be fixed based on the PDF of pixel intensity such that only a small fraction α of pixels in the image (1, 5 or 10 %) will be affected. Specifically, the lower threshold, $P_{\alpha/2}$, can be defined as the $\alpha/2$ percentile of the PDF of pixel intensities; the upper threshold, $P_{100-\alpha/2}$, can be defined as the $100 - \alpha/2$ percentile of the PDF of pixel intensities.

Image pixel intensity, $I(x, y)$, is then modified as follows:

$$\text{if } I(x,y) < P_{\alpha/2} \text{ then } I_{\text{trim}}(x,y) = P_{\alpha/2} \tag{10}$$

$$\text{if } I(x,y) > P_{100-\alpha/2} \text{ then } I_{\text{trim}}(x,y) = P_{100-\alpha/2} \tag{11}$$

$$\text{else } I_{\text{trim}}(x,y) = I(x,y) \tag{12}$$

Changes in pixel intensity reduce (reset) the variability of intensity values of pixel belonging to the darkest (the brightest) areas of the image. Finally, image intensity is mapped (linearly) from $P_{\alpha/2}$–$P_{100-\alpha/2}$ into the reference intensity range 0–255 increasing the contrast between dark and bright areas.

In this work, image intensity adjustment was made using $\alpha = 1$ %. The proper value of α depends on image quality and can be fixed basing on an objective measure of image-processing performance. If $I(x, y)$ is the 2-D map of pixel intensity of the raw image and $I_{\text{trim},\ \alpha}(x, y)$ is the pixel intensity after image processing when the α level of correction is applied, image-processing performance can be evaluated as [see Hosseini and Naghsh-Nilchi (2012) and Weeratunga and Kamath (2003) among others]:

$$\text{MSE}(\alpha) = \frac{\sum_{(x,y)} \left(I(x,y) - I_{\text{trim},\alpha}(x,y)\right)^2}{\sum_{(x,y)} I(x,y)^2} \tag{13}$$

The value of α minimizing MSE(α) is the best value of the parameter preserving the information content stored in the intensity of the image.

High-frequency noise removal by median filtering

Median filtering is widely used to reduce the random noise scattered over a uniform background (Kiger and Pan 1999). In this work, the median filter is performed by convolving a square two-dimensional filter stencil of width δ over all the pixels within the image. For each position (pixel), the median of gray-level values of pixels within the stencil is evaluated and used to modify the local intensity. The appropriate filter size (δ) for each application depends on the size on the image of the objects which should be preserved by the filter. In our work, the size of tracer particles for the specific arrangement of the test (camera resolution, magnification and focus) is about 4 pixel, and any filter size smaller than 4 pixels will preserve the tracers in the filtered image.

To identify the optimal filter size, we used again the normalized MSE as an image-processing performance index. This time, prior to median-filtering, artificial noise [Gaussian with standard deviation 20 %, as reported in Weeratunga and Kamath (2003) or salt and pepper noise] is added to images. The MSE is defined as a function of the size δ of the median filter:

$$\text{MSE}(\delta) = \frac{\sum_{(x,y)} \left(I(x,y) - I_{\text{med.filt.},\delta}(x,y)\right)^2}{\sum_{(x,y)} I(x,y)^2} \tag{14}$$

The size of the filter which minimizes MSE(δ) is the most appropriate filter size to be used.

Binarization

In the binarization step, a grayscale image is transformed into a black and white image according to the following rule:

$$\text{if } I(x,y) < I_{\text{bw}} \text{ then } I_{\text{bin}}(x,y) = 0 \tag{15}$$

$$\text{else } I_{\text{bin}}(x,y) = 255 \tag{16}$$

The appropriate binarization threshold, I_{bw}, can be determined considering again the variation of the image-processing performance index when different values of I_{bw} are considered. In this work, we define the optimal value of the binarization threshold as the one for which

$$\text{MSE}(I_{\text{bw}}) = \frac{\sum_{(x,y)} \left(I(x,y) - I_{\text{bin},I_{\text{bw}}}(x,y)\right)^2}{\sum_{(x,y)} I(x,y)^2} \tag{17}$$

is minimum.

References

Bernstein O, Shapiro M (1994) Direct determination of the orientation distribution function of cylindrical particles immersed in laminar and turbulent shear flows. J Aerosol Sci 25(1):113–136

Carlsson A, Lundell F, Soederberg L (2007) Fibre orientation control related to papermakings. J Fluids Eng 129(4):457–465

Carlsson A, Hakansson K, Kvick M, Lundell F, Soderberg L (2011) Evaluation of steerable filter for detection of fibers in flowing suspensions. Exp Fluids 51(4):987–996

Cheng Y, Pothos S, Diez F (2010) Phase discrimination method for simultaneous two-phase separation in time-resolved stereo piv measurements. Exp Fluids 49(4):1375–1391

Fitzgibbon A, Pilu M, Fischer R (1999) Direct least squares fitting of ellipse. IEEE Trans Pattern Anal Mach Intell 21(5):476–480

Gillissen J (2008) Polymer flexibility and turbulent drag reduction. Phys Rev E 78(4):046311

Holm R, Soederberg D (2007) Shear influence on fibre orientation: dilute suspension in the near wall region. Rheol Acta 46: 721–729

Hosseini S, Naghsh-Nilchi A (2012) Medical ultrasound image compression using contextual vector quantization. Comput Biol Med 42:743–750

Jacob M, Unser M (2007) Design of steerable filters for feature detection using canny-like criteria. IEEE Trans Pattern Anal Mach Intell 26(8):1007–1019

Khalitov D, Longmire E (2002) Simultaneous two phase piv by two parameter discrimination. Exp Fluids 32(2):252–268

Kiger K, Pan C (1999) Two-phase piv for dilute solid/liquid flow. In: Third international workshop on PIV, Santa Barbara, pp 157–162

Kiger K, Pan C (2000) Piv technique for the simultaneous measurement of dilute two-phase flows. J Fluid Eng 122:811–818

Krochak P, Olson J, Martinez D (2008) The orientation of semidilute rigid fiber suspensions in a linearly contracting channel flow. Phys Fluids 20(7):073303

Krochak P, Olson J, Martinez D (2009) Fiber suspension flow in a tapered channel: the effect of flow/fiber coupling. Int J Multiph Flow 35(7):676–688

Krochak P, Olson J, Martinez D (2010) Near-wall estimates of the concentration and orientation distribution of semi-dilute rigid fibre suspension in poiseuille flow. J Fluid Mech 653: 431–462

Kvick M, Hakansson K, Lundell F, Soderberg L, Wittberg LP (2010) Fibre streaks in wall bounded turbulent flow. In: 7th International conference on multiphase flows Tampa, Florida

Lundell F, Soderberg L, Alfredsson P (2011) Fluid mechanics of papermaking. Annu Rev Fluid Mech 43:195–217

Marchioli C, Soldati A (2002) Mechanism for particle transfer and segregation in a turbulent boundary layer. J Fluid Mech 20: 169–201

Marchioli C, Salvetti M, Soldati A (2008) Some issues concerning large-eddy simulation of inertial particle dispersion in turbulent bounded flows. Phys Fluids 20:040603

Marchioli C, Fantoni M, Soldati A (2010) Orientation, distribution and deposition of elongated, inertial fibres in turbulent channel flow. Phys of Fluids 22(3):033301

Metzger B, Butler J, Guazzelli E (2007) Experimental investigation of the instability of a sedimenting suspension of fibres. J Fluid Mech 575:307–332

Mortensen P, Andersson H, Gillissen J, Boersma B (2008a) Dynamics of prolate ellipsoidal particles in a turbulent channel flow. Phys Fluids 20:093302

Mortensen P, Andersson H, Gillissen J, Boersma B (2008b) On the orientation of ellipsoidal particles in a turbulent shear flow. Int J Multiph Flow 34(7):678–683

Moses K, Advani S, Reinhardt A (2001) Investigation of fibre motion near solid boundaries in simple shear flow. Rheol Acta 40: 296–396

Parsa S, Guasto J, Kishore K, Ouellette N, Gollub J, Voth G (2011) Rotation and alignment of rods in two-dimensional chaotic flow. Phys Fluids 23:043302

Parsheh M, Brown M, Aidun C (2005) On the orientation of stiff fibres suspended in turbulent flow in a planar contraction. J Fluid Mech 545:245–269

Parsheh M, Brown M, Aidun C (2006) Variation of fiber orientation in turbulent flow inside a planar contraction with different shapes. Int J Multiph Flow 32(12):1354–1369

Paschkewitz S, Dmitropoulos C, Hou Y, Somandepalli V, Mungalm M, Shaqfeh E, Moin P (2005) An experimental and numerical investigation of drag reduction in a turbulent boundary layer using a rigid rodlike polymer. Phys Fluids 17(8):085101

Picciotto M, Marchioli C, Reeks M, Soldati A (2005) Statistics of velocity and preferential accumulation of micro-particles in boundary layer turbulence. Nucl Eng Des 235:1239–1249

Raffel M, Willert C, Kompenhans J (2002) Particle imaging velocimetry: a practical guide, 2nd edn. Springer, Berlin

Rose KA, Meier JA, Dougherty GM, Santiago JG (2007) Rotational electrophoresis of striped metallic microrods. Phys Rev E 75(1): 011503

Rose KA, Hoffman B, Saintillan D, Shaqfeh ESG, Santiago JG (2009) Hydrodynamic interactions in metal rodlike particle suspensions due to induced charge electroosmosis. Phys Rev E 79(1):011402

Sakakibara J, Wicker R, Eaton J (1996) Measurements of particle fluid velocity correlation and the extra dissipation in a round jet. Int J Multiph Flow 22(5):863–881

Stanislas M, Okamoto K, Kahler C, Westerweel J, Scarano F (2008) Main results of the third international piv challenge. Exp Fluids 45:27–71

Weeratunga S, Kamath C (2003) Comparison of pde-based non-linear anistropic diffusion techniques for image denoising. Image Process Algorithms Syst II Proc SPIE 5014:201–212

Zhang H, Ahmadi G, Fan F, McLaughlin J (2001) Ellipsoidal particles transport and deposition in turbulent channel flows. Int J Multiph Flow 27(6):971–1009